INSTITUT DE FRANCE
Académie des sciences

Comptes Rendus

Mécanique

Xuezhou Lu, Jean-Marc Cherfils, Grégory Pinon, Elie Rivoalen, Olivier Kimmoun and Jérôme Brossard

SPH numerical computations of wave impact onto a vertical wall with experimental comparisons

Volume 349, issue 1 (2021), p. 117-143

Published online: 4 March 2021

https://doi.org/10.5802/crmeca.72

Les Comptes Rendus. Mécanique *sont membres du Centre Mersenne pour l'édition scientifique ouverte*
www.centre-mersenne.org
e-ISSN : 1873-7234

Comptes Rendus
Mécanique
2021, 349, nº 1, p. 117-143
https://doi.org/10.5802/crmeca.72

Short paper / *Note*

SPH numerical computations of wave impact onto a vertical wall with experimental comparisons

Xuezhou Lu [a], Jean-Marc Cherfils [b], Grégory Pinon [*, a], Elie Rivoalen [a, b], Olivier Kimmoun [c] and Jérôme Brossard [a]

[a] Laboratoire Ondes et Milieux Complexes, Normandie Univ, UNIHAVRE, CNRS, LOMC, 76600 Le Havre, France

[b] Laboratoire de Mécanique de Normandie, Normandie Univ, INSA Rouen, LMN, 76000 Rouen, France

[c] Institut de Recherche sur les Phénomènes Hors Équilibre, Centrale Marseille, AMU, CNRS, IRPHE, 13000 Marseille, France

E-mails: xuezhou.lu@gmail.com (X. Lu), jean-marc.cherfils@insa-rouen.fr (J.-M. Cherfils), gregory.pinon@univ-lehavre.fr (G. Pinon), elie.rivoalen@insa-rouen.fr (E. Rivoalen), olivier.kimmoun@centrale-marseille.fr (O. Kimmoun), jerome.brossard@univ-lehavre.fr (J. Brossard)

Abstract. In order to assess wave impacts on coastal structures that are coupled with a marine energy device, for instance an oscillating water column (OWC), a smoothed particle hydrodynamics (SPH) software named JOSEPHINE (Cherfils *et al.*, 2012) is used. In the present study, only a vertical wall will be considered as the front wall or draft of an OWC. In order to clearly identify impact phenomena, a breaking solitary wave will be used, so as to have a single phenomenon. And comparisons with experimental results issuing from Kimmoun *et al.* (2009) will be used as a matter of validation of our numerical study on solitary wave impacts.

The present paper will focus first on the accuracy and convergence of wave propagation within the SPH framework, as a continuation of the work of Antuono *et al.* (2011), both for a regular wave train and for a solitary wave. For regular waves, the second-order dispersion relation is well recovered, up to the third order for the higher amplitudes. For solitary waves, comparisons with analytic and experimental results are also performed.

Several types of impact are obtained similarly to those mentioned in the literature by changing the wave-maker parameters or the water depth in numerical wave flume. However, most of the effort was used for the validation of an impact case well documented in the literature. New experimental results issuing from the previous study of Kimmoun *et al.* were also used. Some intense and rapid impact phenomena are reproduced with our SPH single-phase numerical approach. The conclusion of this work is that a two-phase compressible approach is finally necessary to accurately compute such phenomena.

* Corresponding author.

Keywords. Smoothed particle hydrodynamics, Pressure impact, Solitary wave, Weakly compressible approach, Propagation.

Manuscript received 20th July 2020, revised 11th January 2021 and 17th January 2021, accepted 19th January 2021.

1. Introduction

In the framework of the national project EMACOP (Energie MArine COtiêre et Portuaire) funded by the French Ministry of Ecology, Sustainable Development and Energy, the feasibility of adding wave-energy devices onto coastal protection structure was investigated. This project focuses on multi-functional structures equipped with a coastal wave-energy recovery device. In fact, following the catastrophic consequences of the Xynthia and the global tendency of sea-level rise, France, with more than 3400 km of coast lines, launched a large programme in order to assess the quality of its national coastal protection devices. It is anticipated that there will be a need of increasing the height of the dikes, leading to massive investments. In the meantime, while these coastal protection structures will be refurbished, it could be time for adding wave-energy devices onto these coastal protection devices, such as in the dikes of Mutriku (see Torre-Enciso *et al.* [1]). It is the "best time" for several reasons. First, because heavy refurbishments are necessary and engineering is required to design the new protections structure. It will enable the design engineer to take into account from the start the inclusion of the wave-energy converters. Second, as heavy works will be necessary to repair, or in some cases, reconstruct the dikes, unitary cost reductions (both for the dike reparation or wave-energy device installation) could be obtained using a mutual use of the field work machines and workers. Finally, it is the "best time" because public money is becoming less abundant. And repairing and maintaining such coastal protection structures reveal to be very costly [2]. So, with a (moderate?) increase of the investment costs, it is possible to transform the situation from a purely costly coastal protection device to an earning money situation with wave-energy devices added on the same coastal protection devices. Of course, all these assertions need to be evaluated first in order to ascertain that these wave-energy devices will produce energy on the estimated lifetime of the protection structure, and second that the payback times of the additional investment (wave-energy devices and their installations) are well evaluated.

One of these preliminary studies could deal with the survivability of such wave-energy devices in regular and extreme wave conditions. When evaluating the device survivability in high or extreme weather conditions, impacts of energetic waves have to be considered. In fact, in Neumann *et al.* [3], it is reported that huge hole appeared in the carapace of the full-scale experimental Oscillating Water Column (OWC) of Pico (Açorces, Portugal). One possible explanation could be that the concrete walls were not sufficiently well designed (choice of the concrete, etc.) or manufactured (errors in the fabrication processes). Another possible explanation is that the regular and/or extreme waves impact pressures were underestimated. These underestimations leading to premature fatigue of the device, here the draft of the OWC, and then a possible destruction of the whole device. This practical problem of wave impact involves complicated free-surface deformations. Smoothed particle hydrodynamics (SPH) is an ideal approach to simulate such a process due to its mesh-free, Lagrangian numerical scheme. This numerical approach is commonly used in numerical modelling of wave–structure interactions [4–7]. In the study of Madhi and Yeung [8], weakly compressible SPH (WC-SPH) scheme was used to evaluate the breaking waves exciting forces on asymmetrical wave-energy converters, for the purpose

of improving their survivability. In a similar context, the extreme loads on moving flaps of wave-energy converter were numerically analysed by Marrone *et al.* [9] using both the two-dimensional (2D) and three-dimensional (3D) SPH-flow solver. Very recently, Altomare *et al.* [10] used an SPH-based open source code (DualSPHysics) to model the interaction between sea waves and the Pont del Petroli pier in Spain, which was heavily damaged in January 2020 during the storm Gloria. It aimed to assess wave loading on structure in the context of reconstruction of the pier.

On the one hand, for a similar purpose, an initial stage of water waves propagation should be carried out through simple case configurations. This open-sea ideal situation must be well performed in order to accurately propagate the wave conditions to our structure, and thus, far away from the wave generation. This implicitly means that the solver has very good energy conservation properties. Although it could be seen as trivial, only a very small energy dissipation may deteriorate the propagation phase. But this is an important requirement of any computational fluid dynamics (CFD) software willing to evaluate coastal processes. Regarding the literature, the work from different authors evaluate these kind of simulations using SPH with experimental comparison as Antuono *et al.* [11] or focusing on the energy dissipation as Antuono *et al.* [12]. On the other hand, the complexity arises when the wave overturns or breaks producing strong deformations of the interface. Furthermore, if the fluid is encountering a structure during this process, it will develop high dynamic loads which should be accurately captured by the solver. When this occurs, the air compressibility may play a role depending on the wave breaking. This phenomenon has been a matter of study using two-phase SPH solver by Guilcher *et al.* [13] for instance. But generally speaking, the accuracy of computed impact pressure still being a scientific issue (see for instance Mokrani *et al.* [14, 15] or Rafiee *et al.* [16]), such study dealing with the validation of computed impact pressures are still necessary.

Water wave impacts have been studied for long time mainly from two different motivations. The naval industry have had a great interest in the so-called sloshing problem in liquefied natural gas carriers, where shallow water condition inside the oscillating liquid tanks usually lead to breaking waves impacts on the internal walls. Besides this, the second main field of interest are the extreme pressure records linked to waves impacts on near-shore defensive structures, usually seen as problematic for coastal engineers. There are many experimental pieces of work on this topic since Bagnold [17], who presented the high pressure peaks recorded from real breakwater data in Dieppe Harbor (see De Rouville *et al.* [18]). Laboratory small-scale experiments have been carried out by Hattori *et al.* [19] or Oumeraci *et al.* [20] to name two of the most relevant. The problem has been also examined in a large-scale environment, for example, by Bullock *et al.* [21] or Hofland *et al.* [22]. Moreover, special emphasis on the dynamics and kinematics of the compressibility effects have been presented by Lugni *et al.* [23, 24].

The following section will deal with a detailed description of the WC-SPH solver that is used in the present paper. Sections 3 and 4 will respectively deal with regular wave and solitary wave propagation and the associated conservation properties. The wave impacts, more closely related to the practical problem mentioned above, are presented in the final Section 5. A numerical wave maker generates a solitary wave, which propagates in a wave flume, over a slope beach and finally starts to break on a wall. The impact pressures and run-up on the wall are thus presented and analysed in comparison with experimental results.

2. Weakly compressible SPH model

For all the computations run in the present paper, the WC-SPH solver named JOSEPHINE is used. All the numerical details are described in Cherfils *et al.* [25]. The governing equations are the

Euler equations in the Lagrangian frame for a weakly compressible and inviscid fluid. The Tait's equation of state is used to close the system of equations

$$P_i = \frac{\rho_0 c_0^2}{\gamma}\left(\left(\frac{\rho_i}{\rho_0}\right)^{\gamma} - 1\right), \tag{1}$$

where P_i, ρ_i represent the pressure and the density of the particle, respectively. ρ_0 is the density at the free surface, $\gamma = 7$ is the polytropic characteristic exponent of the fluid, and c_0 is the numerical sound speed. In our model, the smoothing kernel η_ϵ^0 is a truncated Gaussian function proposed by Colagrossi and Landrini [26].

2.1. *Diffusive terms*

Different variants of the diffusive term ($\mathscr{D}_i$) to be added to the continuity equation (2) were proposed in the SPH literature as

$$\frac{\mathrm{D}\rho_i}{\mathrm{D}t} = -\rho_i \sum_j \mathbf{u}_{ij} \cdot \nabla_i \eta_\epsilon^0(\mathbf{x}_{ij}) \frac{m_j}{\rho_j} + \mathscr{D}_i. \tag{2}$$

The present formulation uses the Rusanov flux as a diffusive term which can be expressed as follows:

$$\mathscr{D}_i = \sum_j \psi_{ij} \mathbf{n}_{ij} \cdot \nabla_i \eta_\epsilon^0(\mathbf{x}_{ij}) \frac{m_j}{\rho_j}, \tag{3}$$

with $\mathbf{x}_{ij} = \mathbf{x}_j - \mathbf{x}_i$, $\mathbf{u}_{ij} = \mathbf{u}_j - \mathbf{u}_i$, $\mathbf{n}_{ij} = \mathbf{x}_{ij}/|\mathbf{x}_{ij}|$.

Following the work of Ferrari *et al.* [27], the remaining term ψ_{ij} can be written as

$$\psi_{ij} = c_{ij}(\rho_j - \rho_i - \Delta\rho_{ij}), \tag{4}$$

where $c_{ij} = \max(c_i, c_j)$, $c_i = \sqrt{\partial P_i/\partial\rho_0} = c_0(\rho_i/\rho_0)^{\gamma-1/2}$. $\Delta\rho_{ij}$ is a corrective hydrostatic term to prevent excessive mass fluxes in the fluid [28], this term should be set to zero when gravity is neglected.

Another approach of the diffusive term is proposed by Antuono *et al.* [29] and ψ_{ij} can be written as follows:

$$\psi_{ij} = \delta c_0 \epsilon \left(\frac{2(\rho_j - \rho_i)}{|\mathbf{x}_{ij}|} - \frac{\langle\nabla\rho\rangle_i^L + \langle\nabla\rho\rangle_j^L}{\mathbf{n}_{ij}}\right), \tag{5}$$

where δ is the coefficient for controlling the intensity of the diffusion ($\delta = 0.1$ here), $\langle\nabla\rho\rangle_i^L$ is added to denormalise density gradient [30]. This last formulation, combined with an artificial viscosity term (see Section 2.2), is called δ-SPH. Compared with the term of Ferrari *et al.*, δ-SPH is compatible with the hydrostatic solution but pressure fields are less smooth for short-time dynamics problems, as mentioned in the paper of Antuono *et al.* [31]. To conclude on this, in the present paper, only the Rusanov flux in the version of Ferrari *et al.* [27] will be used.

2.2. *Artificial viscosity term*

In many SPH studies published in the literature, an artificial viscosity [32] is added to the pressure term of the momentum equation (6), in order to stabilise the scheme and reduce spurious oscillations

$$\frac{\mathrm{D}\mathbf{u}_i}{\mathrm{D}t} = \sum_j \left(-\frac{P_j + P_i}{\rho_i} + \underbrace{\frac{\alpha^* \epsilon c_0 \rho_0}{\rho_i}\pi_{ij}}_{\text{artificial viscosity}}\right) \nabla_i \eta_\epsilon^0(\mathbf{x}_{ij}) \frac{m_j}{\rho_j} \tag{6}$$

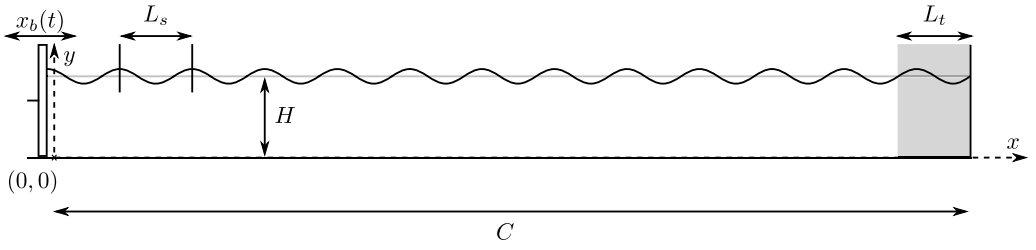

Figure 1. Schematic view of the numerical wave flume of length C, with a still water height H. A piston wave maker is installed on the left-hand side, its horizontal motion $x_b(t)$ (depending on f, the oscillation frequency and a, the amplitude) generates regular wave of wavelength L_s. A damping zone is defined on the right-hand side, its length is equal to L_t, the theoretical wavelength issuing from (13).

with $\pi_{ij} = (\mathbf{u}_{ij}\cdot\mathbf{x}_{ij})/|\mathbf{x}_{ij}|^2$ and α^* being the artificial viscosity coefficient, which is classically set to 0.02. For the cases of wave propagation and impact, the artificial viscosity is not used for the reason of energy dissipation. As the wave propagation is relatively a long process, the conservation of energy should be taken into consideration.

In summary, the system of equations used in our numerical study in this paper is

$$\begin{cases} \dfrac{\mathrm{D}\rho_i}{\mathrm{D}t} = -\rho_i \sum_j \mathbf{u}_{ij}\cdot\nabla_i \eta_\epsilon^0(\mathbf{x}_{ij})\dfrac{m_j}{\rho_j} + \mathscr{D}_i & \text{Continuity} \\ \dfrac{\mathrm{D}\mathbf{u}_i}{\mathrm{D}t} = -\dfrac{1}{\rho_i}\sum_j (P_j+P_i)\nabla\eta_\epsilon^0(\mathbf{x}_{ij})\dfrac{m_j}{\rho_j} + \vec{g} & \text{Momentum} \\ P_i = \dfrac{\rho_0 c_0^2}{\gamma}\left(\left(\dfrac{\rho_i}{\rho_0}\right)^\gamma - 1\right) & \text{Tait's equation} \\ \quad + \text{boundary conditions} \end{cases} \tag{7}$$

The time advancing scheme is a fourth-order Runge–Kutta and a CFL condition is defined as

$$CFL = \frac{\delta t c_0}{\epsilon}, \tag{8}$$

where δt is the time step and ϵ is our smoothing parameter defined as $\epsilon = 1.33\,\delta x$. In the following computations, the space discretisation δx is the same in the x- and y-coordinate.

3. Regular wave propagation

3.1. *Wave generation*

The considered domain is an open wave flume, as those already used in several other experimental studies such as [33]. Figure 1 depicts a scheme of a 2D side view of the wave flume. A piston-type wave maker enables the generation of regular wave of frequency $f = 1/T = \omega/2\pi$ (T being the period and ω the corresponding pulsation); the wave-maker amplitude is denoted by a. The wave flume walls are considered with a slip condition, numerically enforced with the *ghost particles* technique [34, 35]. The wave-maker horizontal motion $x_b(t)$ is defined by the following equation:

$$x_b(t) = \begin{cases} a\sin\left(\dfrac{\omega}{4k}t\right)\sin(\omega t) & \text{if} \quad t < kT \\ a\sin(\omega t) & \text{else.} \end{cases} \tag{9}$$

By a simple derivation, the wave-maker horizontal velocity is obtained, this velocity being useful for the enforcement of the *ghost particle* technique. Figure 2a shows the obtained wave-maker motion by applying (9). A transient increase is applied on the wave-maker velocity for

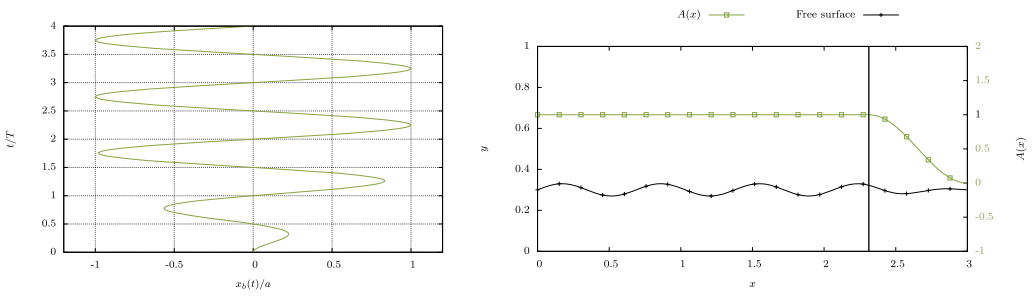

(a) Wave-maker motion. (b) Absorbing conditions.

Figure 2. Left: graphical representation of the piston-type wave maker $x_b(t)$ as a function of time. The transient increase is applied on 2 period ($k = 2$). Right: absorbing conditions by direct modification of the particles' acceleration.

k periods (generally $k = 2$ is used), which enables a nice and smooth initialisation of particles motion at the start of the computation.

3.2. *Absorbing conditions*

For the study of wave interaction with any obstacle, being an experimental or a numerical study, incoming waves need to be damped or absorbed to avoid reflected waves to perturb the observation zone. Here, at the right-hand side of the wave flume (see Figure 1), a damping zone is used with a length L_t, this length being equal to fundamental wavelength of the computed wave. Therefore, for all the particles situated in this damping zone, their acceleration is modified as the following at the end of the time step:

$$\frac{\mathrm{D}\mathbf{u}_i}{\mathrm{D}t}^* = A(x_i)\frac{\mathrm{D}\mathbf{u}_i}{\mathrm{D}t} \tag{10}$$

with

$$A(x_i) = \begin{cases} 1 & \text{if } x_i < C - L_t \\ \sin^2\left(\dfrac{(C-x_i)\pi}{2L_t}\right) & \text{else.} \end{cases} \tag{11}$$

Figure 2b represents the applied function $A(x)$ to the particle depending on their position in the wave flume (x being their first Cartesian coordinate $\mathbf{x}$). This function $A(x)$ continuously decreases to 0 when the particles come closer to the wave flume extremity, progressively reducing their displacement and movement.

3.3. *Regular wave propagation with SPH*

This technique of wave absorption is very cost-effective in terms of CPU resources and it was applied to four different wave conditions presented in Table 1. The imposed wave-maker frequencies were 1.25 Hz, 1.5 Hz, 1.75 Hz, and 2 Hz. The dispersion relation, issuing from the Stokes model, enables the calculation of the wavelength for a given wave period T and water depth H. The second-order Stokes theory gives a wavelength of

$$L_t = \frac{gT^2}{2\pi}\tanh\left(2\pi\frac{H}{L_t}\right), \tag{12}$$

Table 1. Theoretical wavelengths at the second (L_t) and third ($L_{t,3}$) orders and the computed wavelength (L_s) for each of the four wave configurations

f (Hz)	L_s (m)	L_t (m)	$L_{t,3}$ (m)	$\frac{L_s-L_t}{L_t}$	$\frac{L_s-L_{t,3}}{L_{t,3}}$	$\frac{a_h}{L_s}$
1.25	0.967	0.962	0.978	0.6%	−1.2%	0.021
1.5	0.697	0.689	0.711	1.1%	−2%	0.029
1.75	0.523	0.509	0.54	2.7%	−3.2%	0.038
2	0.412	0.39	0.431	5.6%	−4.4%	0.049

Relative errors with respect to both of the theoretical wavelength is also indicated together with the camber. For all cases, the generated wave amplitude is $a_h = 0.02$ m.

and at the third order, an additional term depending on the wave camber $a_h/L_{t,3}$ is used with a_h being the emitted wave amplitude

$$L_{t,3} = \frac{gT^2}{2\pi}\tanh\left(2\pi\frac{H}{L_{t,3}}\right)\left[1+\left(\frac{2\pi a_h}{L_{t,3}}\right)^2\frac{9+8\cosh^4\left(2\pi\frac{H}{L_{t,3}}\right)-8\cosh^2\left(2\pi\frac{H}{L_{t,3}}\right)}{8\sinh^4\left(2\pi\frac{H}{L_{t,3}}\right)}\right]. \tag{13}$$

The other geometrical parameters of the wave flume are: $a = 0.01$ m, $H = 0.3$ m, and $C = 3$ m. The computations were run with the following numerical parameters: a fourth-order Runge–Kutta (RK4) time integration scheme, 50×500 particles initially positioned in the flume, a time step of $\Delta t = 0.0002$ s, and a numerical sound speed of $c_0 = 10\sqrt{gH}$.

Figure 3 shows a spatio-temporal deformation of the free surface for each of the four test configurations and detailed in Table 1. The considered time interval is $[0;20T]$ and the deformed free surface is only presented on this usable flume length, that is to say $x \in [0; C-L_t]$, after removal of the absorbing beach. From these images, no reflected wave can be observed on the incident waves. A discussion on the reflection rate will be presented in the following paragraphs but it can already be observed that it will be rather weak. Another interesting feature of these images presented in Figure 3 is that the transient phase can clearly be identified and it clearly depends on the wave frequency, the longer transient phases for the higher frequencies.

Figure 5 represents the free-surface envelops obtained from the SPH computed wave fields from $t/T = 15$ to $t/T = 20$ for one wave configuration presented in Table 1. From an observation of these envelopes, the reflection rate of an obstacle or a damping beach can be deduced. By evaluating the maximum thickness $H_{\max}$ of the envelop (zone with the maximum deformation of the free surface) corresponding to an antinode and a node (zone with the minimum deformation of the free surface) hereafter called $H_{\min}$ ahead of the black line in Figure 4, an approximation of the reflection rate is then possible. An antinode and a node are separated with a distance of $L_s/4$ in the absence of harmonics of the fundamental mode. From the presented results of Figure 5, it is very difficult to identify these nodes and antinodes on the whole length of the wave flume, except for the lower frequency $f = 1.25$ Hz. As a consequence, an assessment of the reflection rate led to a value smaller than 5% in this precise case. Another technique, such as the one of Mansard and Funke [36] with several probes, would have led to a similar value. On the contrary, the absence of modulation in the free-surface envelopes indicates that the reflection rate is zero, which is not exactly the case neither.

From these computations (see Table 1), the effective wavelength L_s can be recalculated from the numerical results and the obtained wavelengths slightly differ from the theoretical second-order theory (12). The different second L_t and third $L_{t,3}$ order wavelength together with the recalculated L_s ones are presented in Table 1 as a matter of comparison. A graphical representation of these results is presented in Figure 6. From these results, it can be observed

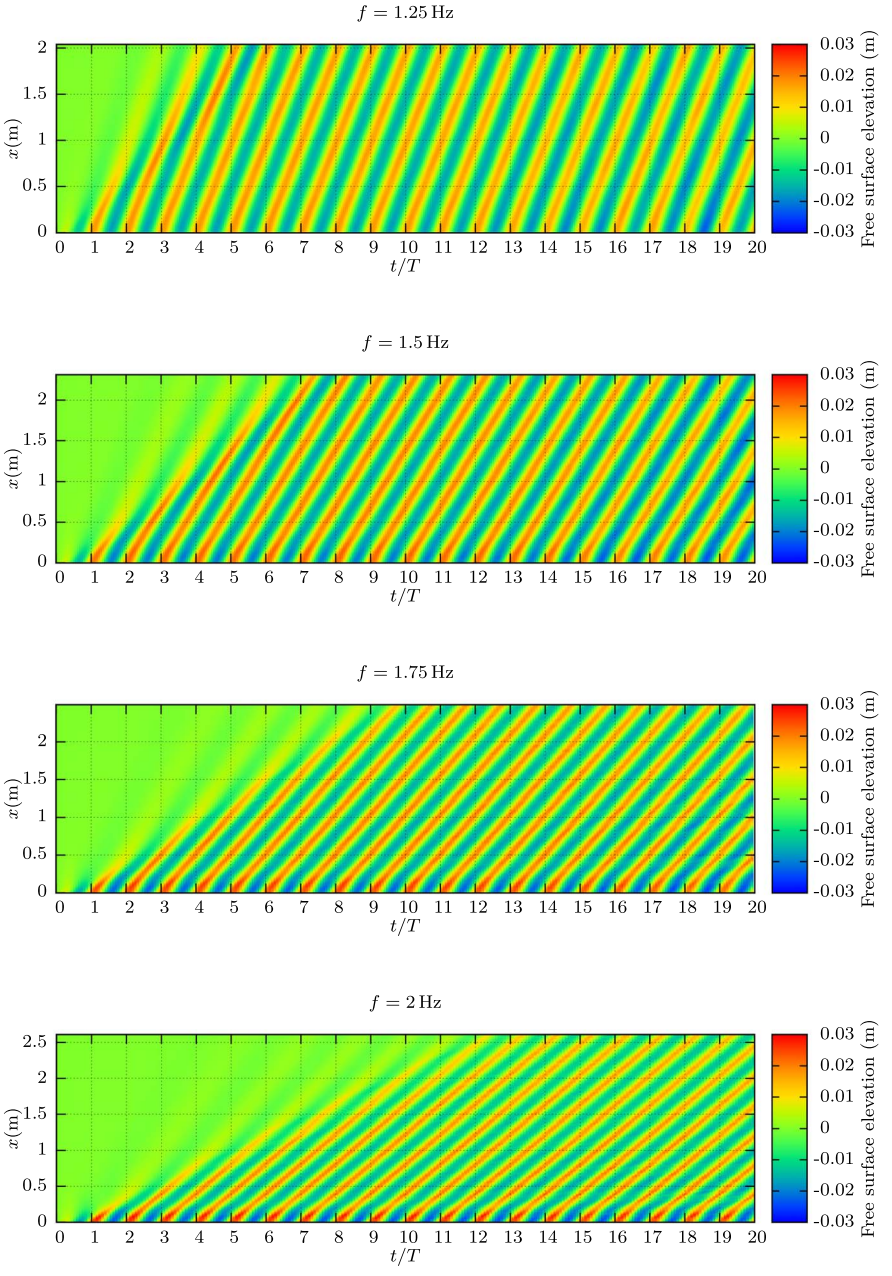

Figure 3. Spatio-temporal free-surface deformation for the four studied different wave periods indicated in Table 1. $t/T \in [0;20]$ and $x \in [0; C - L_t]$.

that the obtained L_s wavelengths show a fairly good agreement with both second- and third-order theory. The second-order theory generally overestimate the recalculated value while the third-order theory underestimate these values. Several reasons may be invoked to explain these differences:

- The four computed waves, all have the same amplitude, as a consequence, the camber increase with wave frequency (in that respect, a small free-surface overelevation can be

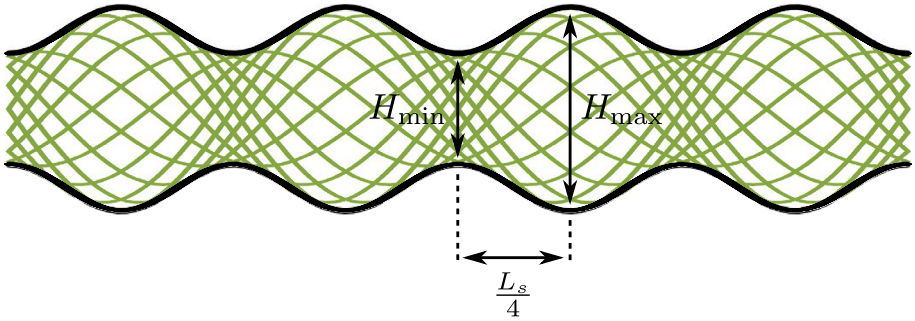

Figure 4. Schematic representation of the reflection rate with the methods of nodes and antinodes.

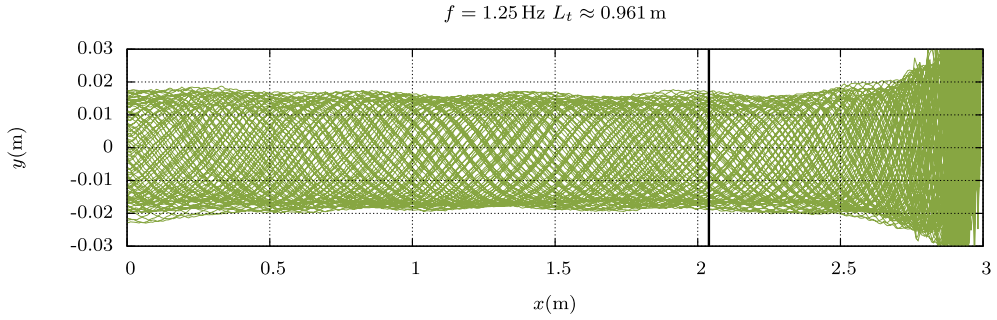

Figure 5. Free-surface envelops between $t/T = 15$ and $t/T = 20$, for one computed wavelengths presented in Table 1. The black line indicates the beginning of the wave absorption zone as described above in equation (10) of Section 3.2.

observed in the vicinity of the wave maker for $f = 1.75$ Hz and $f = 2$ Hz as it can be observed in Figure 3. Another case was then computed for $f = 1.75$ Hz with a smaller amplitude of $a = 0.005$ m. The recalculated wavelength from the computation is then $L_s = 0.51$ m, giving an error of 0.26% (all other parameters unchanged) with this new wave amplitude of $a_h = 0.01$ m. The third-order curve was added on Figure 6 to illustrate the camber effect on the computed waves, the obtained SPH results being situated in between the two theoretical curves.

- The total number of particle is identical whatever the wave-maker frequency is. Therefore, the number of particle per wavelength (the ratio L_s/h) decreases with increasing frequency. This last phenomenon could possibly explain a degradation of the results for higher frequency, especially the wave amplitude reduction as the wave propagate for $f = 1.75$ Hz and $f = 2$ Hz. An analysis of the impact of this ratio L_s/h on the conservation properties of computed waves could be envisaged.

4. Solitary wave propagation and rebound

After having validated the regular wave propagation, a similar validation will be performed for solitary wave or soliton. In fact, as the aim of the study is to perform a single impact event, a solitary wave is thus taken into account in the following. By definition, a soliton is a self-propagating single wave that maintains its shape and amplitude during its propagation for a uniform bathymetry. From a more general point of view, this soliton's propagation property over

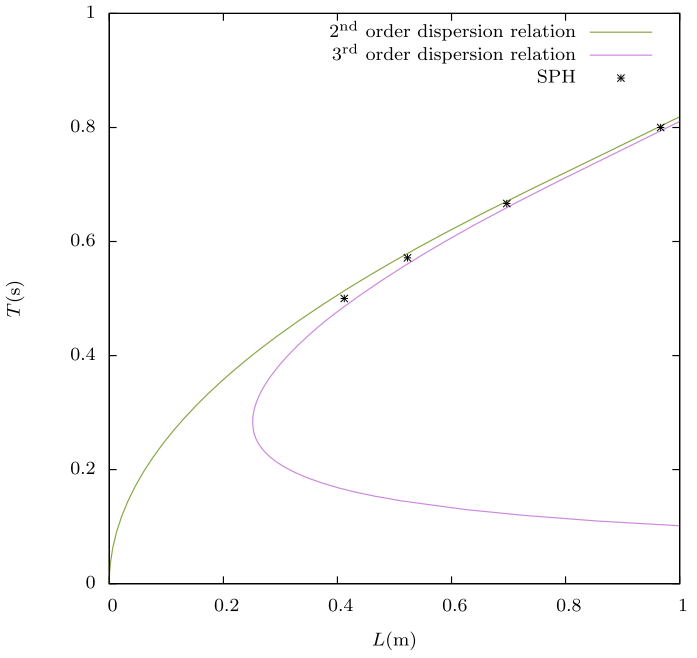

Figure 6. Comparison between the second- and third-order Stokes theory and the recalculated wavelength from the computations for the four configurations presented in Table 1 and for the wave amplitude $a_h = 0.02$ m.

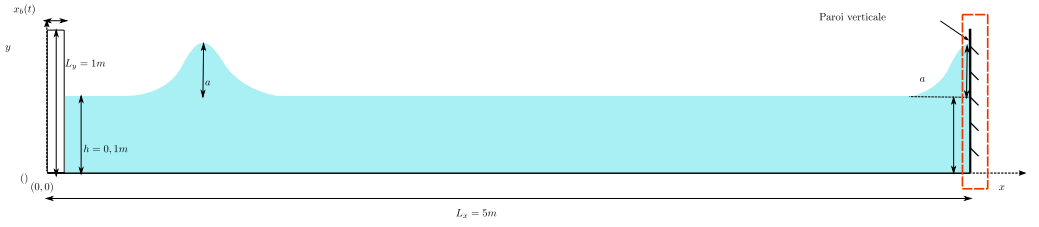

Figure 7. Schematic representation of the numerical wave fume used for solitary wave propagation and rebound. Geometrical parameters are defined for generation and propagation (left) and rebound configurations (right).

long distances explains why tsunamis can travel very far away from the location where they were generated. In this section, the generation and propagation of solitons are studied.

4.1. *Solitary wave generation and propagation*

Figure 7 depicts the schematic diagram of the studied configuration: a soliton is generated by a piston-type wave maker at the left-hand side of the flume. The wave flume is $L_x = 5$ m length, $L_y = 1$ m height with a water depth of $h = 0.1$ m. The fluid density is set to $\rho_0 = 1000\,\mathrm{kg/m^3}$ and the gravity value is set to $g = 9.81\,\mathrm{m/s^2}$. The numerical sound speed is set so that $c_0 = 10\sqrt{g(a+h)}$. $x_b(t)$ represents the wave-maker displacement for generating a solitary wave. The first-order

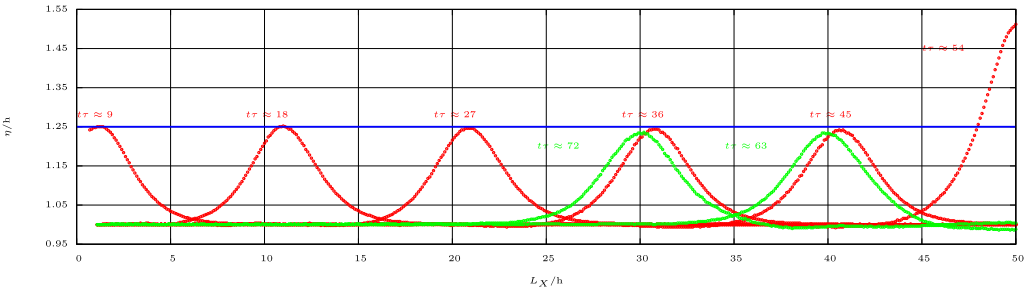

Figure 8. The propagation of a soliton with $a = 0.025$ m and $h = 0.1$ m. Red curves indicate the free surfaces before rebound and green curves indicate the moments after the rebound. The time t is made dimensionless by $\tau = \sqrt{g/h}$.

theory of solitary wave proposed by Goring [37] will be used, based itself on the theory of Boussinesq [38]. The imposed wave-maker displacement can be written as

$$x_b(t) = \frac{a}{kh}[\tanh(k(ct - x_b(t)) + \tanh k\lambda)], \tag{14}$$

where c is the soliton velocity, a is its amplitude, $k = \sqrt{3a/4h^3}$ and $\lambda = 3.8h/k$ are two additional parameters. This is an implicit equation that is solved numerically by Newton's method. The theoretical soliton celerity (denoted by c) was given up to higher orders by Wehausen and Laitone [39] in the following form:

$$c = \sqrt{gh}\left[1 + \frac{1}{2}\frac{a}{h} - \frac{3}{20}\left(\frac{a}{h}\right)^2 + \cdots\right]. \tag{15}$$

A first-order approximation of this celerity was proposed by Boussinesq [38] and L. Rayleigh [40], which is used for our numerical simulations:

$$c = \sqrt{gh\left(1 + \frac{a}{h}\right)}. \tag{16}$$

The differences between the results obtained by (15) and (16) remain insignificant for ratios of $a/h < 0.4$. In this work, this condition will be respected for most of the computed configurations except for some computations of Section 4.3.

In order to observe the conservation of total energy during the soliton propagation, its amplitude is studied over time. Figure 8 describes the soliton free surfaces at different instants, before and after its rebound. The horizontal axis represents its position in the wave channel. The blue line is the theoretical wave crest for this soliton of amplitude $a = 0.025$ m. Figure 8 shows that the soliton maintains its amplitude while it propagates, equivalent to a weak energy loss. When the wave crest reaches the wall, the water level begins to increase and it continues to increase until it reaches a maximum. This maximum value is greater than twice the soliton amplitude, as mentioned in Power *et al.* [41]. This value is also indicated by the curve at instant $t\tau \approx 54$ in Figure 8 with $\tau = \sqrt{g/h}$. Then the water level begins to decrease and the wave crest propagates in the opposite direction. It can be observed that its amplitude decreases about 5.6% after rebound.

4.2. *Numerical convergence*

In order to validate the convergence properties of the used numerical code for modelling of the soliton, a spatial and time convergence analysis was performed. First, the various simulations presented in Table 2 were carried out in order to ensure the numerical convergence of the presented computations. Two criteria were used for verifying convergence; first the maximum

Table 2. The parameters for the various simulations

a (m)	a/h	C_0 (m/s)	N_x	N_y	δx (m)	δt (s)	CFL
0.025	0.25	1.107	2000	40	0.0025	1.5×10^{-4}	0.4996
0.025	0.25	1.107	2500	50	0.0020	1.2×10^{-4}	0.4996
0.025	0.25	1.107	3333	67	0.0015	1.0×10^{-4}	0.4996
0.025	0.25	1.107	5000	100	0.0010	6.0×10^{-5}	0.4996
0.030	0.30	1.129	2000	40	0.0025	1.5×10^{-4}	0.5095
0.035	0.35	1.151	2000	40	0.0025	1.5×10^{-4}	0.5192
0.040	0.40	1.172	2000	40	0.0025	1.5×10^{-4}	0.5287
0.050	0.50	1.213	2000	40	0.0025	1.5×10^{-4}	0.5472
0.060	0.60	1.253	2000	40	0.0025	1.5×10^{-4}	0.5652
0.070	0.70	1.291	2000	40	0.0025	1.5×10^{-4}	0.5826
0.075	0.75	1.310	2000	40	0.0025	1.5×10^{-4}	0.5911

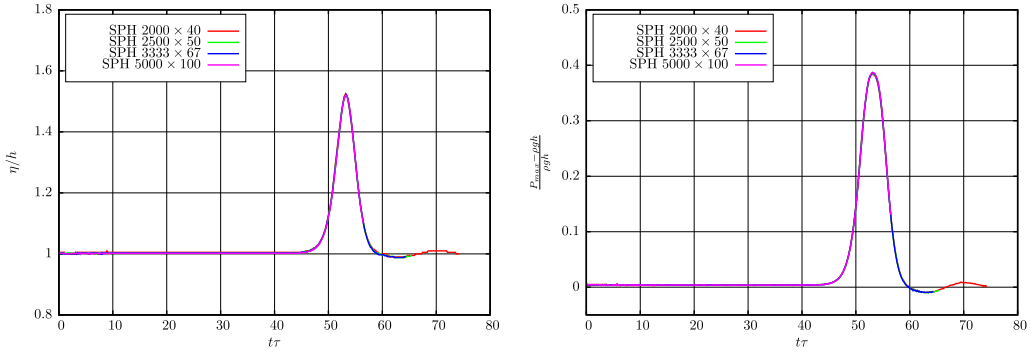

(a) Water level on the wall.

(b) Maximum pressure on the wall.

Figure 9. Convergence study for a non-breaking soliton, where $a/h = 0.25$. Time is adimensionalised so that $t\tau = t\sqrt{g/h}$.

water level at the opposite wall, and second the maximum pressure on the same wall. These criteria are rather complicated to achieve as they are measured at the opposite side of the soliton generation, that is to say that very accurate propagation properties are necessary. Different discretisations (i.e., different inter-particles distances) were used and are shown in the upper part of Table 2. The obtained results are presented in Figure 9. The two Figures 9a and b demonstrate a good spatial convergence of our scheme. From these two graphs, it can be observed that a very nice convergence is obtained for the four used discretisations on the given configuration. The four curves of the free-surface elevation η/h (Figure 9a) or dimensionless pressure (Figure 9b) quasi superimpose. The duration of the four simulations in each figure are different, that is the reason why these curves end at different times. From these very nice results, it can be concluded that convergence is obtained for the range of used discretisations. Then the soliton amplitude will be varied in order to analyse some physical properties of soliton propagation in the framework of the approximate solution for the solitary wave given in (14).

4.3. *Varying the soliton amplitude*

From a certain amplitude to water-depth ratio (a/h), the soliton naturally starts to break but the threshold is not of common agreement in the literature. Therefore, different amplitudes were

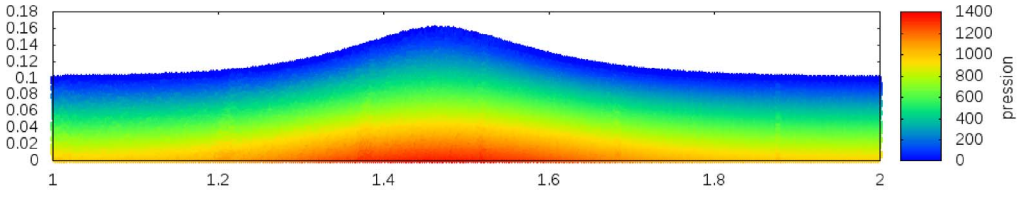

(a) A soliton of $a/h = 0.6$

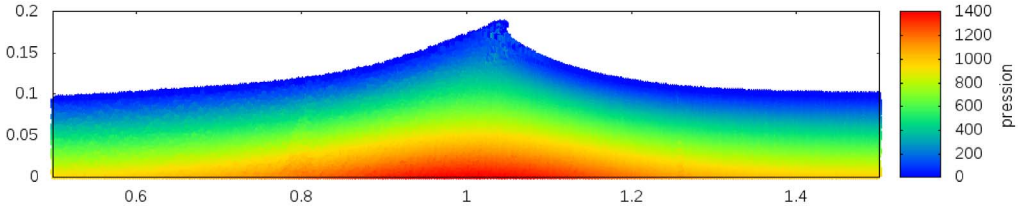

(b) A soliton of $a/h = 0.75$

Figure 10. Two solitons with different values of a/h. For $a/h = 0.75$, the soliton breaks up during its propagation.

numerically tested and the parameters are given in the lower part of Table 2. As the soliton amplitude given for the simulation (a in (14)) increases, the soliton crest height increases too. A change of regime appears when a/h reaches a limit which corresponds to the case where the fluid particle velocities situated at the crest are equal to or greater than the soliton celerity (16). This change of regime can lead to wave breaking as shown in the lower part of Figure 10 for $a/h = 0.75$. According to a study of Bougis [42], using this approximation given in (16), J. M'Cowan [43] showed that the ratio between the wave height and the water depth is always less than 0.78. Other values at the wave breaking point, ranging from 0.73 to 1, were calculated by different authors. In order to determine this threshold in our simulations, the same water height $h = 0.1$ m will be kept and the different amplitude of the soliton a will be taken. In our computations, starting from $a/h = 0.75$, the change of regime is reached, as that can be seen in Figure 10b. The soliton breaks up before it meets the wall. This shows that the threshold value for wave breaking is less than 0.78, most likely between ≈ 0.70 and 0.75 in our simulations.

The Figures 11a and b describe respectively the water height and the maximum pressure on the wall against the time for different a/h values. The double peak curve observed for the pressure from $a/h \geq 0.4$ (Figure 11b) has already being reported by Chambarel *et al.* [44, 45]. It was indicated to be due to the residual falling jet. In Figure 12, the maximum water height on the wall obtained by our SPH simulations are compared with different analytical, numerical, and experimental data which are presented in the article by Power and Chwang [41]. Except for an isolated experimental point around $a/h = 0.1$ of Chan *et al.*, all these results are greater than those predicted by the linear theory which gives the maximum amplitude equal to twice the initial amplitude of the wave. Our results are in very good agreement with the solution of Byatt-Smith *et al.* [46] when $a/h \leq 0.4$. They are between the analytical solution and the numerical solution of Power when $a/h > 0.4$. More recent works of Chambarel *et al.* [45] and Chen *et al.* [47] also studied such a configuration but for higher values of a/h, higher than 0.5. In such a configuration, the maximum water height unsurprisingly overestimates the linear theory, but their numerical results correspond to the experimental ones (Chambarel *et al.* [44, 45] for instance). These last studies focused on the jet formation and run-up for these higher values of a/h.

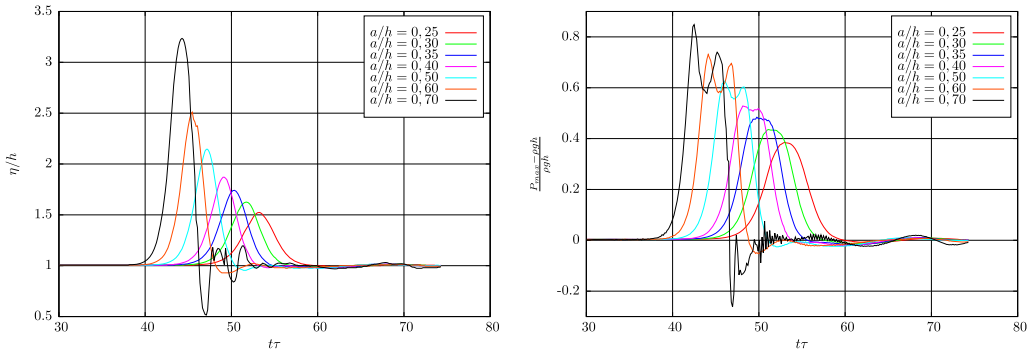

(a) Water Height (b) Pressure

Figure 11. The temporal evolution of the water height and the maximum pressure on the wall. Time is adimensionalised by $t\tau = t\sqrt{g/h}$.

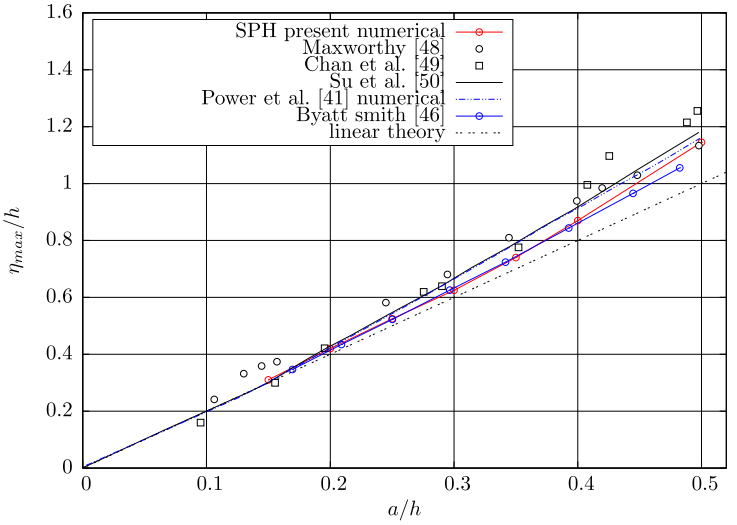

Figure 12. Maximum water height on the wall in terms of a/h.

As previously stated, the remainder of this study concerns solitons with small ratios of the wave amplitude to water depth ($a/h \lesssim 0.1$). A sloped beach will be added to the right end of the wave flume in our modelling (Figure 13a). As a result, the wave breaking is triggered when the soliton propagates above the sloped beach where the local water depth decreases.

5. Solitary wave impact onto a vertical wall

SPH methods have been extensively used to study impacts on solid materials. For example, the parallel solver SPH-flow developed by HydrOcean and École Centrale Nantes was applied in the context of sloshing impacts by Oger *et al.* [48], by coupling the FSID software of Scolan *et al.* [49] with an SPH–ALE method to compute the wave generation and the impact phenomenon, respectively. In order to model the influence of air bubbles during the impact, a bi-fluid version has been developed by Guilcher *et al.* [13]. More recently, a similar study of wave impact together

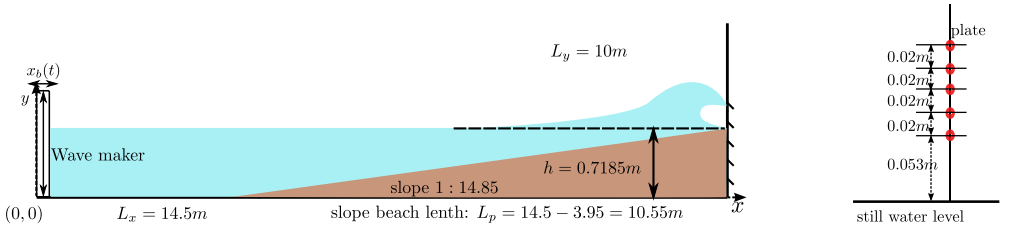

(a) Numerical domain

(b) Arrangement of pressure sensors [53]

Figure 13. Schematic sketch of breaking solitary wave onto a vertical wall in a numerical wave flume with sloping beach.

with an ISOPE test case was carried out by Rafiee *et al.* [16], who discussed the complexity of such impact cases and the difficulty to obtain accurate converged results.

5.1. *Description of the solitary wave impact test case*

With similar goals, but in the aim to apply the developed software to a survivability study of wave-energy devices built onto coastal dykes or wave breakers, the impact of a solitary wave onto a vertical wall will now be studied. But at first, validation of wave impacts onto a vertical wall will be carried out to compute more realistic and complex geometries and regular or irregular wave conditions. It is well known that assessing the pressure during an impact at a fixed position in a wall is rather complicated. In fact, it is very sensitive to many factors such as the rapidity of the phenomenon, the possible difference in the impact location between experimental and numerical results, etc. However, this paper will be an attempt to predict pressure distribution on the wall and compare them with previous experimental results. Figure 13a depicts the schematic diagram of the studied configuration: a soliton is generated by the wave maker at the left-hand side of the flume. The generated solitary wave is propagated and travels up to a sloping beach, which eventually makes the wave start to break. Finally, the breaking wave impacts on a vertical wall positioned at the right-hand side of the flume. Figure 13b depicts the arrangement of pressure sensors at the vertical wall, which are located along the centreline of the plate. In order to compare the numerical records with experimental ones, the exact similar configuration as the one used by Kimmoun *et al.* [50] in their experiments will be defined here. Unfortunately, some differences however exist, such as the fact that our computation are 2D (for computational cost mainly), whereas the experiments are obviously performed in 3D. And the numerical wave maker is the same piston-type wave maker as presented in previous Section 4, whereas the experimental wave maker is an oscillating flap. Finally, this will be discussed at the end of this section, the impacted vertical wall have some flexibility in the experiments with two small vertical gaps on each side (to allow the wall oscillate during wave impact), whereas the present numerical wall is fixed and rigid. Computations of the flexible behaviour of the impinged wall was out of the scope of this study. For instance, Khayyer *et al.* [51] performed an impressive and interesting study on that particular topics. Elastic or moving structures are in fact a common concern in coastal wave impact problems. In Marrone *et al.* [9], the comparison between blocked (fixed and rigid flap) and non-blocked (freely moving flap) configurations was investigated to evaluate the torque. It confirmed that the wave impact loads were much larger when the structure is fixed. In a similar way, the present study with a fixed and rigid wall intends to highlight maximum wave impact loads that could be encountered in similar configurations.

To give more details, the wave flume is L_x = 14.5 m long with a slope beach of L_p = 10.55 m (see Figure 13a). The experimental water depth is h = 0.71044 m and a beach is inclined with

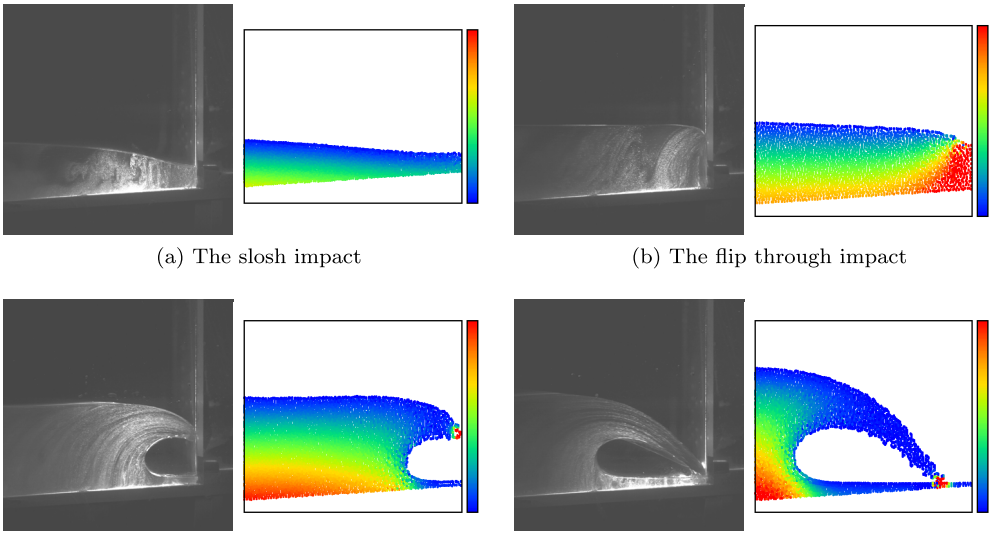

(a) The slosh impact (b) The flip through impact

(c) The air pocket impact (d) The aerated impact

Figure 14. Different types of impact obtained experimentally by Kimmoun *et al.* at École Centrale Marseille (black and white pictures, the experimental campaign is presented in [52]) and the similar impact configuration numerically reproduced with the present SPH model (coloured images).

a slope of 1:14.85, both experimentally and numerically. Other numerical parameters are the fluid density, set to $\rho_0 = 1000$ kg/m^3 and the acceleration due to gravity set to $g = 9.81$ m/s^{-2}. The numerical sound speed is set to $c_0 = 10\sqrt{g(a+h)}$. On Figure 13a, $x_b(t)$ represents the wave paddle displacement for generating a solitary wave. Similarly to the previous Section 4, the same law (14) is defined for calculating the wave paddle displacement $x_b(t)$.

Several validation studies were already performed with the present numerical software either for the generation and propagation of wave in a 2D numerical flume [28] or other academic impact configurations [53,54]. By varying the water depth and/or the soliton amplitude, different types of impact can be obtained. Figure 14 shows four different types of impact (identified and classified by Oumeraci *et al.* [20] or Hull *et al.* [55]) and experimentally observed by Kimmoun *et al.* [52] in their experimental facility at École Centrale Marseille. Thus, in order to obtain the same impact as that in the experiments, the soliton parameters (a and h) have been varied so that to reproduce at maximum the experimental ones [54]. And in fact, the same types of impact can be numerically reproduced by using the present SPH implementation as shown in Figure 14.

Experimental studies indicate that both the flip through and the air-pocket impact are capable of creating high pressures (see Hattori *et al.* [19] or Bullock *et al.* [21] for instance). The highest impact pressure tend to occur in the flip through impact [19]. However, within an air-pocket impact, the spatial extent and duration of the high pressure region increase, which could cause greater forces exerted by fluid onto the structure [21]. In addition, air-pocket impact is more common in practical problems as flip through impact only exists when the water front is nearly vertical and parallel to the impinged wall, this precise configuration being rather seldom in nature. Therefore, this air-pocket impact (cf. Figure 14c) will be the focused configuration of the following Section 5.2 as it is well documented on the experimental point of view presented in [50,52] plus additional unpublished materials.

5.2. *Focus on an impact case: calibration of wave shape and velocity field*

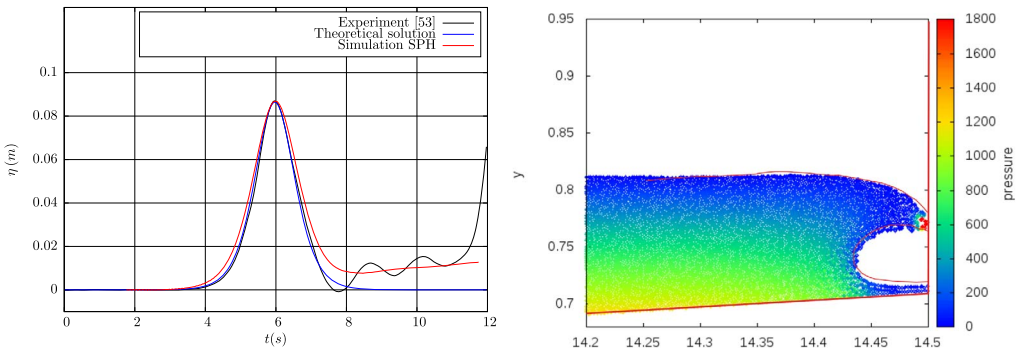

(a) Surface elevation (b) Wave shape

Figure 15. Left: temporal signal of the free-surface elevation at $x = 2.8$ m, the amplitude of the soliton is $a = 0.0864$ m. Right: comparison of the computed (coloured by pressure) and the experimental [50] (red) wave shape at breaking. Computation parameters are $h = 0.713$ m, $a = 0.0864$ m, $d_x = 0.002$ m.

Breaking of a solitary wave depends on the geometry of the wave flume, the water depth h and the soliton amplitude a. Experimentally, the geometrical dimensions of wave flume, the length of the beach, etc. are fixed. Numerically, exactly the same geometrical configuration will be reproduced in the presented numerical computations. The breaking point of the soliton could change only by varying the amplitude a or water depth h. And these two parameters are very sensitive; only a small change in one of these two values completely modify the soliton breaking. Such differences, at the order of a millimetre or less, are in the measurable error range of experimental trials. In addition, the experimental and numerical wave maker are different, that might cause discrepancies in the generated solitons. Again, in order to obtain the same impact as that in the experiments, the soliton parameters (a and h) were chosen so as to reproduce the surface elevation after the soliton generation (Figure 15a), the wave shape (Figure 15b) and the velocity field (Figure 16) with the chosen experimental case of Figure 14c. After several attempts (not presented in the paper) the couple of parameters $h = 0.713$ m and $a = 0.0864$ m provides the better match to the experimental soliton. The results of this soliton computation will be detailed in the following.

The temporal evolution of the free-surface elevation at a fixed point of wave tank ($x = 2.8$ m) is traced in Figure 15a. It is compared with the theoretical solution and the temporal evolution of the free-surface elevation signal recorded in the experiment. Figure 15a shows that the numerical free-surface elevation matches well with the theoretical solution and the experimental result. However, some oscillations can be observed after the crest passes through the sensor ($t \approx 6$ s) in both experimental and numerical results. These oscillations, called dispersive tail, are due to the solitary wave generation, to the truncation of the wavelength which is infinite theoretically. But in practice, it is impossible to generate a wave of infinite wavelength, neither numerically nor experimentally. Except for these last small oscillations, the correlation between the three approaches is very correct and the solitary wave generation can now be considered as validated. Unfortunately, such validation is not enough to accurately reproduce the temporal pressure recorded on the impinged wall. In fact, a small change in this couple of parameters (a and h) could completely change the shape of the wave during breaking and the subsequent impact. Therefore, a calibration of the wave shape was necessary as presented in Figure 15b. Figure 15b

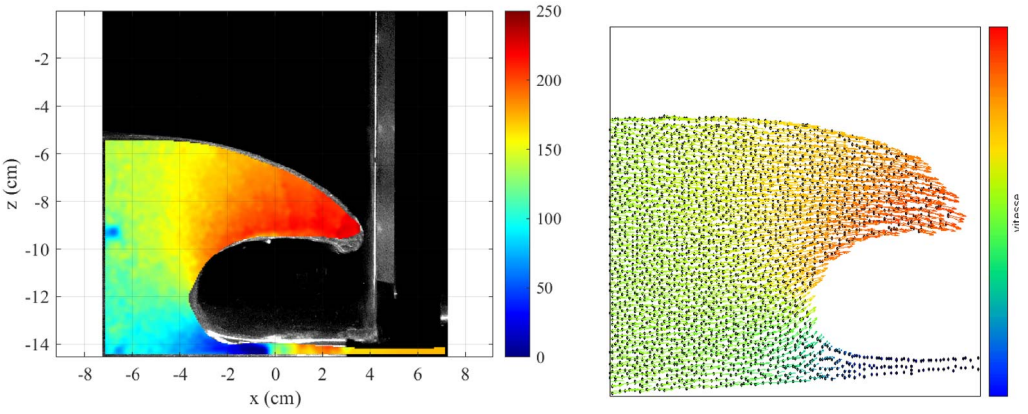

(a) Experimental result (b) Numerical result

Figure 16. Comparison of the velocity fields obtained experimentally and numerically. The experimental setup and measurements techniques are presented in Kimmoun *et al.* [50]. The simulation parameters are: $h = 0.713$ m, $a = 0.0864$ m, $d_x = 0.002$ m.

shows the comparison between experimental (red lines) and numerical wave shape (coloured map) at the time of impact. Very good agreement is obtained here while a small variation at the order of a millimetre or less in a and/or h would have led to a different impact. And thus, different pressure sensors (as presented in Figure 13b) would have been exited leading to completely different pressure records than those presented in Figure 20.

Velocity of an incident wave also has an important role on the impact pressure. Comparison of experimental (Figure 16a) and numerical (Figure 16b) velocity fields at the time that the wave crest begins to hit the wall were performed. Figure 16a shows the velocity field obtained from particle imaging velocimetry measurements. The colour palette is the same in both Figures 16a and b: the velocity magnitude varying from 0 m/s (blue) to 2.5 m/s (or 250 mm/s) (red). The numerical maximum speed is at the tip of the jet and it well corresponds to the result experimentally obtained. The spatial scale of Figure 16a is not exactly the same as the one of Figure 16b, but again the shape of the soliton in these two cases are in good agreement (cf. Figure 15b).

Although run-up is not the goal of this work, it is an important phenomenon in the design of coastal structures. Most of the damage caused from tsunamis are related to their run-up on the coast. Solitary waves are often employed to investigate the characteristics of tsunami [56]. The run-up is defined as the difference between the maximum altitude reached by the wave on a beach or structure and the still water level. Figure 17 shows the comparison of experimental and numerical results of the run-up of a solitary wave of $a = 0.0864$ m. A very correct match between numerical and experimental data is obtained, except for the maximum value. Apart from the differences between experimental configuration and 2D numerical model, the two small vertical gaps on each side of the experimental wall which allow fluid to pass through, could probably explain this difference.

5.3. *Convergence of the results and assessment of the wave impact pressure*

The next two sections will mainly be dedicated to the analysis of the impact pressures and the comparison of the obtained numerical pressure records with the experimental ones. A single wave impact configuration will be presented and analysed, the solitary wave with an amplitude of $a = 0.0864$ m and a water height of $h = 0.713$ m. During the experiments of Kimmoun *et al.* [50],

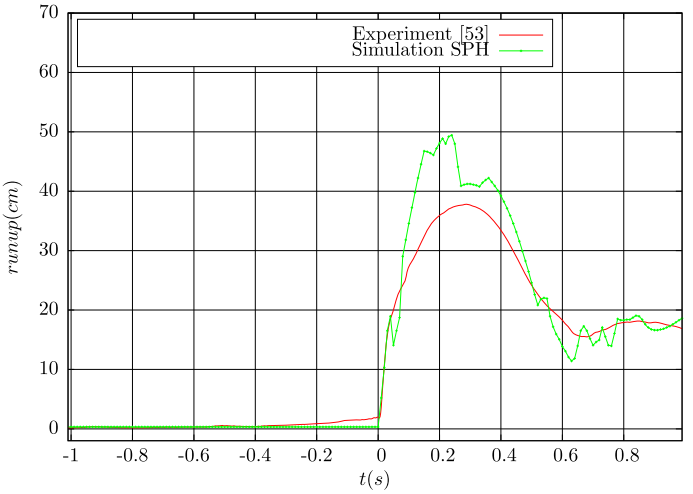

Figure 17. Comparison of the run-up on a vertical wall. The simulation parameters are: $h = 0.713$ m, $a = 0.0864$ m, $\delta x = 0.0025$ m, $CFL = 0.8422$.

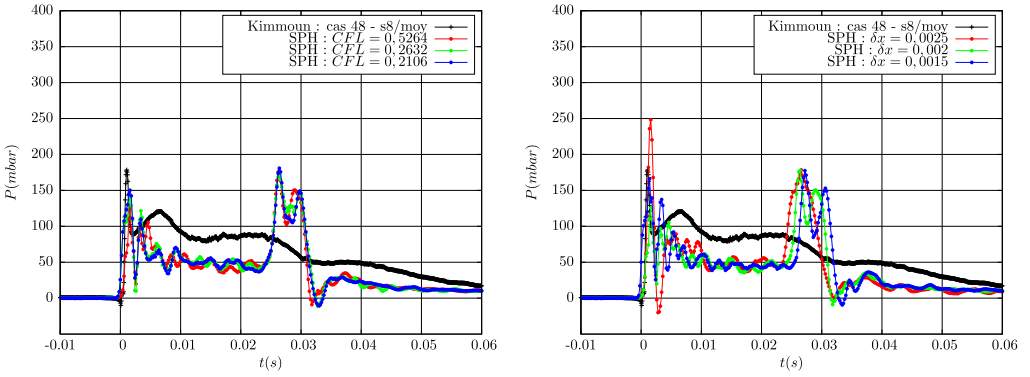

(a) Temporal convergence (b) Spatial convergence

Figure 18. Time evolution of the pressure. Altitudes of the sensors in the experiences of Kimmoun *et al.* [57] is 0.073 m above the beach. $t = t_{\text{sim}} - 8.88$ s. Simulation parameters : $h = 0.713$ m, $a = 0.0864$ m (cf. Table 3). The numerical pressure records were obtained by applying a moving average over 5 δt.

pressure measurements are performed on the opposite wall. And different sensors are located at different altitudes of this plate. To compare with the experimental results, the pressure at different points on the wall will be calculated. However, prior to comparison with the experimental results and analysis of the physical phenomena encountered, a convergence analysis will be carried out. In fact, pressure is a rather sensible physical parameter, and to some extent, even more in the SPH framework. Therefore, this convergence analysis, once performed and validated, will give more confidence in the obtained results.

The two graphs of Figure 18 show the time evolution of the wall pressure during the computation of impact pressure, compared with the results measured by the pressure sensor in the experiments. In these two graphs, the convergence of the scheme is studied by reducing respectively the inter-particle distance and the computation time step. Impact pressure records at three different locations of the wall are compared with the experimental results in the PhD dissertation of

Table 3. Simulation parameters for the convergence study

	h (m)	a (m)	C_0 (m/s)	N_x	N_y	δx (m)	δt (s)	CFL
1	0.713	0.0864	28.00	5800	285	0.0025	1.0×10^{-4}	0.8422
2	0.713	0.0864	28.00	7250	357	0.0020	5.0×10^{-5}	0.5264
3	0.713	0.0864	28.00	7250	357	0.0020	2.5×10^{-5}	0.2632
4	0.713	0.0864	28.00	7250	357	0.0020	2.0×10^{-5}	0.2106
5	0.713	0.0864	28.00	9667	475	0.0015	5.0×10^{-5}	0.7018

Lu [54]. Here, the pressure records for a single probe at 0.073 m above the beach is considered. In both graphs of Figure 18, one can observe that the wave impact happens exactly at the same time for all computations, whatever the spatial or temporal resolution is in Table 3. The propagation phase is then exactly the same and the results are converged in that respect. Then, the first pressure signals ($0. \leq t \leq 0.005$) depict very high oscillations. The first experimental pressure peak ($0. \leq t \leq 0.002$) is reproduced numerically but with more oscillations than experimentally. These numerical oscillations could be caused by the WC approach and also possibly some numerical inaccuracies. These types of acoustic pressure perturbations are a common problem for WC-SPH approaches. Even after using some correction terms or adding an artificial viscosity term, for instance the delta-SPH [29], acoustic noise still exists in the numerical solution. In order to obtain more representable pressure results, Meringolo *et al.* used a filtering technique based on wavelet transform to remove the acoustic components [58]. In our comparisons with experimental results, the numerical pressure fields are not filtered. Only a moving average over 5 δt was performed on the numerical pressure records. In future studies of wave impacts, this filtering technique might be considered. For this very intense and short phenomenon ($0 \leq t \leq 0.005$), a true convergence cannot be completely obtained. However, both for the space and temporal resolutions, the numerical pressure records stay in a fairly reasonable range. Then, passed $t = 0.005$ s, the results are fully converged. The same plateau pressure with $P \approx 50$ mbar is obtained for all discretisations in space and time. For ($0.025 \leq t \leq 0.032$) the numerically high pressure value is exactly reproduced for all the time steps, a small delay can be observed on the graph for spatial converge (Figure 18b) but the pressure value are very similar. As a conclusion, one can estimate that a good convergence of our numerical scheme is obtained in time and in space.

5.4. *Wall impact pressure evaluation and analysis*

The images of the following Figure 19 present several snapshots of the pressure field pressure during several instant of the impact. On these graphs, the three black dots represent the position of three pressure sensors, which are respectively 53 mm, 73 mm, and 93 mm above the beach. Then, the associated pressure records are depicted in Figure 20. The black curves represent the experimental results from Kimmoun *et al.* [50] and the red line the most refined computation with a mesh discretisation of $\delta x = 0.0015$ m, all the other computation parameters being defined in Table 3. Each snapshot, identified by a letter between (a) and (i) on Figure 19, is clearly indicated by a vertical line on the temporal pressure records (Figure 20) enabling an easy comparison.

The first pressure peak obtained in the experiment is rather well represented numerically, especially by the sensor at 73 mm. In this very short duration (about 0.0025 s, between (b) and (c)) when the wave spike first impacts on the wall, the experimental and numerical results are in a relative accordance: the magnitude of the experimental peak is $\approx$ 170 mbar, whereas two or three peaks between $\approx$175 mbar and 265 mbar are obtained numerically. In fact, the SPH numerical computations always gave a much noisier pressure records than experimentally. However, considering the above mentioned studies, such a discrepancy could be considered as

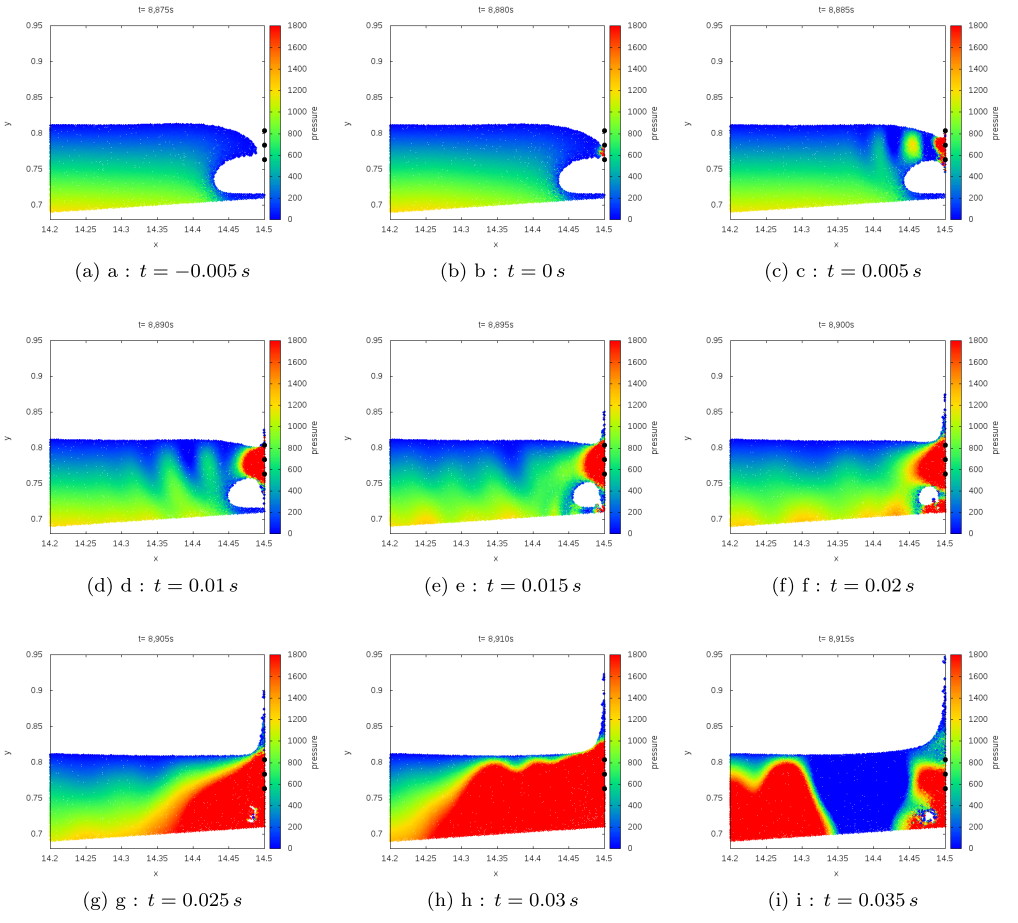

(a) a : $t = -0.005\,s$ (b) b : $t = 0\,s$ (c) c : $t = 0.005\,s$

(d) d : $t = 0.01\,s$ (e) e : $t = 0.015\,s$ (f) f : $t = 0.02\,s$

(g) g : $t = 0.025\,s$ (h) h : $t = 0.03\,s$ (i) i : $t = 0.035\,s$

Figure 19. Wave shape coloured by pressure corresponding to different instants marked by a, b, c, …, i in Figure 20. The numerical parameters are $h = 0.713$ m, $a = 0.0864$ m, $\delta x = 0.0015$ m, $CFL = 0.7018$, $t = t_{\text{sim}} - 8.88$ s (Table 3). The unit of pressure is Pa.

a fair agreement. Then, the lower experimental pressure probe (at 53 mm) depicts a pressure increase between $t \approx 0.0025$ s and $t \approx 0.01$ s (between (b) and (d)) with a maximum pressure at the order of 100 mbar. This pressure increase is much probably due to the compression of the air-cavity entrapped, which could not be considered in our one-phase model. However, from $t \approx 0.005$ s (c) to $t \approx 0.025$ s (g), a very nice pressure plateau with ≈ 50 mbar is numerically obtained mainly at 73 mm. To some extent, this pressure plateau is also well observed at 53 mm and a bit less at 93 mm from the beach. From the different snapshots of Figure 19(c) to Figure 19(f), this can clearly be attributed to the dynamic pressure imposed by the water spike. Indeed, a theoretical dynamic pressure $P_{\text{dyn}} = \rho V^2 \approx 62.5$ mbar calculated from the velocity fields presented in Figure 16 with a characteristic velocity of 2.5 m/s accurately fits with the ≈ 50 mbar and the $\approx$ 65–75 mbar from the two lower pressure gauges. Finally, a second and very high pressure peak suddenly appears (occurring around $0.025\text{ s} < t < 0.03$ s) and with very high magnitudes ($P \approx 250{,}200{,}150$ mbar at respectively at 53 mm, 73 mm and 93 mm). From Figure 19(g), one can observe that the void supposed to be filled of air and representing the air-cavity suddenly disappears creating a very high and spurious pressure field numerically. The pictures (g), (h), and (i) from Figure 19 correspond to the instants when the second peak occurs. But in the

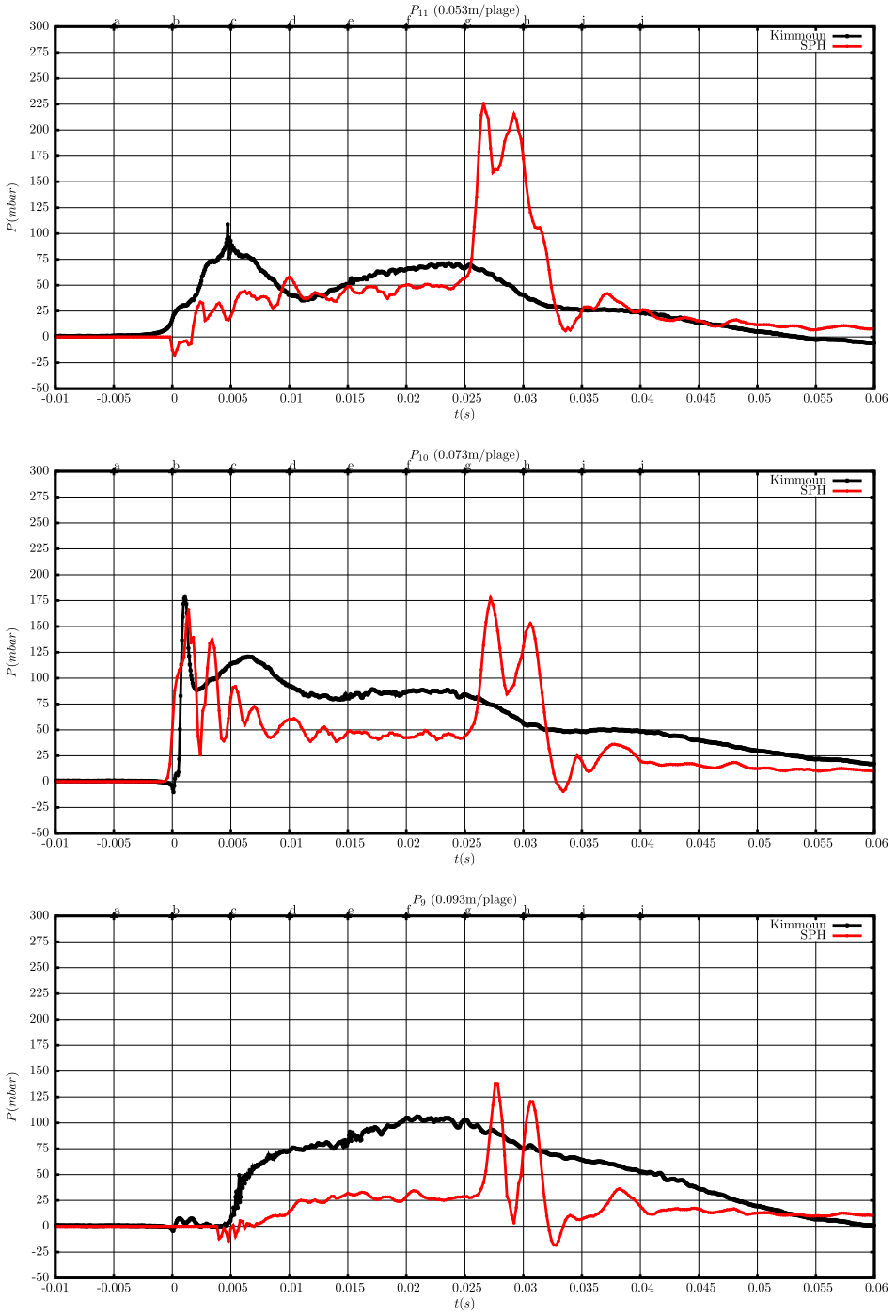

Figure 20. The comparison between the experimental and numerical impact pressure at 53 mm, 73 mm, and 93 mm above the beach. The numerical parameters are $h = 0.713$ m, $a = 0.0864$ m, $\delta x = 0.0015$ m, $CFL = 0.7018$, $t = t_{\text{sim}} - 8.88$ s (Table 3). The numerical pressure records were obtained by applying a moving average over $5\delta t$.

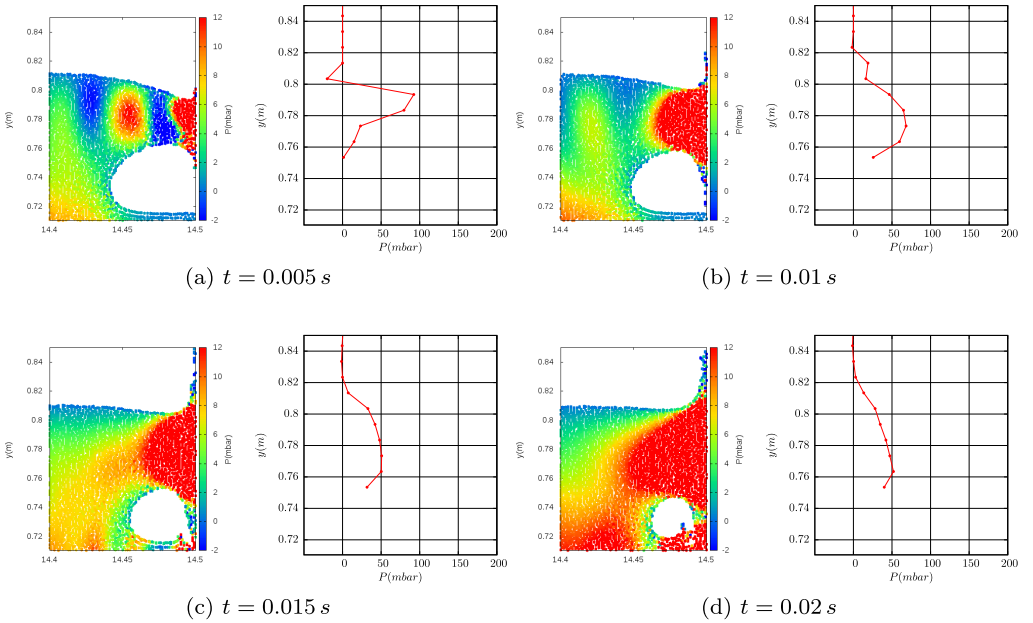

(a) $t = 0.005\,s$ (b) $t = 0.01\,s$

(c) $t = 0.015\,s$ (d) $t = 0.02\,s$

Figure 21. Wall pressure distribution at different instants during the impact. The numerical parameters are $h = 0.713$ m, $a = 0.0864$ m, $\delta x = 0.0015$ m, $CFL = 0.7018$, $t = t_{\text{sim}} - 8.88$ s (Table 3).

experiments, this air pocket plays its role and slowly vanishes most probably due to the air evacuating by the two backlash as indicated by Kimmoun *et al.* [50]. Hence, the second pressure peak in Figure 20 is most probably due to the effect that only a single-phase model is considered in these computations. The influence of the air pocket on the impact pressures has been studied both experimentally and analytically [19, 59]. In order to treat the air compressibility, the two-phase SPH model was implemented and presented in the PhD dissertation of Lu [54]. With the use of this two-phase SPH model, the second pressure peak of Figure 20 disappeared between (f) and (h). However, even if this air pocket could be more accurately reproduced with the two-phase model, other numerical problems were encountered, such as wave overturning during the propagation phase and a large increase of the CPU cost. In more recent works, such as the one in the work of Batlle Martin *et al.* [60], 2D and 3D two-phase compressible and incompressible solvers are used to treat similar experimental configurations, with interesting result too.

In order to answer the initial question that was studying the dynamic loads of waves impinging on coastal protection structures, possibly equipped with wave-energy device, a couple of conclusion can be drawn. First, Figure 21 depicts the pressure distribution on the vertical wall during different instants of impact. These pressure distributions at different instant during the impact represent much valuable pieces of information, when the solver ability to accurately reproduce pressure level is validated. Following this precise study and the above mentioned results, the used SPH solver proved that the convergence of numerical pressure records could be achieved. The use of a single even, such as a soliton's impact, could clearly identify the advantage and drawbacks of the used numerical solver. Beyond the fact that the pressure record converge, the accuracy of the reproduced pressure was fairly good when the air compressibility was not playing a major role. Unfortunately, in the present air-pocket impact, air compressibility could not be neglected; first because the pressure features of the compression of the air pocket are not reproduced, and

second because spurious behaviours are obtained when the voids are collapsing. However, SPH solvers could still be nice candidates for such studies, provided a two-phase model is used, which could possibly be SPH-flow, GPUSPH, or DualSPHysics for instance. But other approaches such as Eulerian volume of fluid formulation could also well apply, see for instance, Batlle Martin *et al.* [60]. And, when wave-energy converters will be deployed on coastal protection structures, an energy assessment will be needed most probably using CFD solvers. Once these numerical models being set up for the energy assessment, these CFD solvers could also be used for survivabilty assessments.

6. Conclusion

This paper presented some applications of the SPH code JOSEPHINE [25] in order to assess impact pressure for a solitary wave impinging a vertical wall. The choice of solitary wave was made to have a single event so that the impact phenomenon could be more easily identified than if it was a wave train impinging a similar wall. This study was performed in order to validate this SPH approach for further analysis of wave-energy converters survivability when installed on coastal protection devices. This study was first initiated in the framework of the French national project EMACOP, funded by the French Ministry of Ecology, Sustainable Development and Energy.

To start with, the different stages of wave impinging a coastal structure were studied independently: a regular wave train propagation, a solitary wave propagation and then a solitary wave breaking and impinging a vertical wall. Wave generation and propagation was one of the first application of the developed SPH software during the PhD dissertation of Cherfils [28]. The used one-phase WC-SPH solver proved to be very accurate when propagating a regular wave train over a distance of several wavelengths, ≈ 20 in the used wave flume. The reproduced wavelength and wave period were accurately in accordance with the second- and third-order Stokes theory, tending to the third order for the shortest wavelengths as the theory would expect. And, with the used wave maker (a piston-type wave maker) and the defined absorbing beach, only a very small reflection rate could be estimated.

Then, similar accurate propagation properties were identified for solitary waves of different amplitudes. The ratio of soliton's amplitude over water depth for which the solitary wave was starting to break naturally was estimated by this numerical approach and proved to be in accordance with the previous experimental and numerical works of the literature. Then, the properties of such solitary wave rebound on a vertical wall was also evaluated and proved to be very accurate with respect to the literature, for instance with respect to the work of Byatt-Smith *et al.* [46].

Then, following the validation of the propagation properties, the impact of a solitary wave on a vertical wall in a numerical wave tank was addressed. Once again, the implemented SPH model proved to converge on the generated solitary wave and the free-surface elevation just before the wall were superimposing for the different tested mesh discretisations. Then, different wave breaking configurations were obtained, but a special attention to the air-pocket impact was paid as one of the most impulsive impact case. Such air-pocket impact configurations were studied during the experimental work of Kimmoun *et al.* [50, 52], providing ideal test cases for numerical–experimental comparison. These validations were performed on the surface elevation (water wave spike form before impact), velocity fields, and wave run-up onto the wall. But, in the aim of assessing impact pressure, the time evolution of different pressure sensor installed onto the vertical wall were recorded and compared to their experimental counterparts. Some of the impact features were correctly reproduced by the SPH solver, such as the very first impact peak (although it was much noisier in the numerics) and the subsequent water spike dynamic

pressure plateau. The absence of gaseous phase was anticipated to have an influence on the quality of the numerical results, the quantification of this influence being one of the major goal. Unfortunately, the absence of air phase proved to have two major consequences on the results. First, the air-pocket compression was absolutely not taken into consideration and a first discrepancy could easily be identified with the experimental records. More recent computations of Batlle Martin *et al.* [60] proved that the account of air compressibility improve the comparison. Second, and probably the most important feature, the collapse of the void creates spurious but very important pressure peaks recorded by all pressure sensors. These consequences are likely to appear in any one-phase solver. Although ignoring the influence of the absence of air phase, the results are satisfactory in terms of numerical convergence and accuracy of the computation of impact pressure. That still encouraged us to develop a two-phase model. As mentioned in Section 5, the implementation of a two-phase SPH model, which is a continuation of the work presented in this paper, was described in the PhD dissertation of Lu [54]. More recently, a two-phase model using another approach was tempted in the work of Batlle Martin *et al.* [60] and more accurate comparisons with the experiments could be acheived. It can be inferred that a two-phase accurate CFD solver could be used when assessing the energy yield and performing a survivability analysis of a wave-energy device installed onto a coastal protection structure. These analyses being performed during the design phase should possibly reduce the cost of such coastal wave-energy devices and also prevent them from failure, for instance, because of holes in the carapace of the Pico wave-energy device as reported by Neumann *et al.* [3].

Acknowledgements

XZL acknowledges the financial support for her PhD grant from the Regional Council of Haute-Normandie. The authors would like to acknowledge the financial support of the CPER-ERDF program DIADEMAR funded by the Normandy Regional Council and the European Union. The authors also would like to acknowledge the national project EMACOP, under which this study was initiated. The present work was performed on computing resources provided by CRIANN (Normandy, France).

References

[1] Y. Torre-Enciso, I. Ortubia, L. L. de Aguileta, J. Marqués, "Mutriku wave power plant: from the thinking out to the reality", in *8th European Wave and Tidal Energy Conference (EWTEC), Uppsala, Sweden*, 2009.

[2] Cerema, "Systmes houlomoteurs bords quai, guide de conception en phase avant-projet", in *Collection: Connaissances., edition cerema eau, mer et fleuves, 134, rue de beauvais 60280 margny-ls-compigne Edition*, 2020.

[3] F. Neumann, I. L. Crom, "Pico owc — the frog prince of wave energy? recent autonomous operational experience and plans for an open real-sea test centre in semi-controlled environment", in *9th European Wave and Tidal Energy Conference (EWTEC), Southampton, UK*, 2011.

[4] R. Dalrymple, B. Rogers, "Numerical modeling of water waves with the SPH method", *Coast. Eng.* **53** (2006), no. 2, p. 141-147, coastal Hydrodynamics and Morphodynamics.

[5] A. Khayyer, H. Gotoh, S. Shao, "Enhanced predictions of wave impact pressure by improved incompressible SPH methods", *Appl. Ocean Res.* **31** (2009), no. 2, p. 111-131.

[6] X. Liu, H. Xu, S. Shao, P. Lin, "An improved incompressible SPH model for simulation of wavestructure interaction", *Comput. Fluids* **71** (2013), p. 113-123.

[7] E. Didier, D. Neves, R. Martins, M. Neves, "Wave interaction with a vertical wall: SPH numerical and experimental modeling", *Ocean Eng.* **88** (2014), p. 330-341.

[8] F. Madhi, R. W. Yeung, "On survivability of asymmetric wave-energy converters in extreme waves", *Renew. Energy* **119** (2018), p. 891-909.

[9] S. Marrone, A. Colagrossi, V. Baudry, D. Le Touzé, "Extreme wave impacts on a wave energy converter: load prediction through a SPH model", *Coast. Eng. J.* **61** (2019), no. 1, p. 63-77.

[10] C. Altomare, A. Tafuni, J. M. Domínguez, A. J. Crespo, X. Gironella, J. Sospedra, "SPH simulations of real sea waves impacting a large-scale structure", *J. Mar. Sci. Eng.* **8** (2020), no. 10, article no. 826.

[11] M. Antuono, A. Colagrossi, S. Marrone, C. Lugni, "Propagation of gravity waves through an SPH scheme with numerical diffusive terms", *Comput. Phys. Commun.* **182** (2011), no. 4, p. 866-877.
[12] M. Antuono, A. Colagrossi, "The damping of viscous gravity waves", *Wave Motion* **50** (2013), no. 2, p. 197-209.
[13] P. Guilcher, G. Oger, L. Brosset, E. Jacquin, N. Grenier, D. Le Touzé, "Simulation of liquid impacts with a two-phase parallel SPH model", in *Proceedings of 20th International Offshore and Polar Engineering Conference, June 20–26, Bejing, China*, 2010.
[14] C. Mokrani, "Impact de vagues déferlantes sur un obstacle vertical. modele théorique et calcul numérique des pics de pression", PhD Thesis, Université de Pau et des Pays de l'Adour, 2012.
[15] C. Mokrani, S. Abadie, K. Zibouche, "Lien entre la forme locale de la surface libre et les pressions d'impact générées par une vague déferlante sur un ouvrage", *Houille Blanche* **6** (2013), p. 53-57.
[16] A. Rafiee, D. Dutykh, F. Dias, "Numerical simulation of wave impact on a rigid wall using a two–phase compressible SPH method", 2013, preprint, https://arxiv.org/abs/1306.0769.
[17] R. A. Bagnold, "Interim report on wave-pressure research. (includes plates and photographs)", *J. Inst. Civil Engr.* **12** (1939), no. 7, p. 202-226.
[18] A. G. de Rouville, P. Besson, P. Pétry, "Etat actuel des études internationales sur les efforts dus aux lames", *Annales Ponts et Chaussees* **108** (1938), no. 7, p. 5-113.
[19] M. Hattori, A. Arami, T. Yui, "Wave impact pressure on vertical walls under breaking waves of various types", *Coast. Eng.* **22** (1994), no. 1, p. 79-114, special Issue Vertical Breakwaters.
[20] H. Oumeraci, P. Klammer, H. Partenscky, "Classification of breaking wave loads on vertical structures", *J. Waterway Port Coast. Ocean Eng.* **119** (1993), no. 4, p. 381-397.
[21] G. Bullock, C. Obhrai, D. Peregrine, H. Bredmose, "Violent breaking wave impacts. part 1: Results from large-scale regular wave tests on vertical and sloping walls", *Coast. Eng.* **54** (2007), no. 8, p. 602-617.
[22] B. Hofland, M. Kaminski, G. Wolters, "Large scale wave impacts on a vertical wall", *Coast. Eng. Proc.* **1** (2011), no. 32, structures–15.
[23] C. Lugni, M. Miozzi, M. Brocchini, O. Faltinsen, "Evolution of the air-cavity during a depressurized wave impact. part i: The kinematic flow field", *Phys. Fluids* **22**, doi:10.1063/1.3407664.
[24] C. Lugni, M. Brocchini, O. M. Faltinsen, "Evolution of the air cavity during a depressurized wave impact. ii. the dynamic field", *Phys. Fluids* **22** (2010), no. 5, article no. 056102.
[25] J. Cherfils, G. Pinon, E. Rivoalen, "JOSEPHINE: A parallel SPH code for free-surface flows", *Comput. Phys. Commun.* **183** (2012), no. 7, p. 1468-1480.
[26] A. Colagrossi, M. Landrini, "Numerical simulation of interfacial flows by smoothed particle hydrodynamics", *J. Comput. Phys.* **191** (2003), no. 2, p. 448-475.
[27] A. Ferrari, M. Dumbser, E. F. Toro, A. Armanini, "A new 3d parallel SPH scheme for free surface flows", *Comput. Fluids* **38** (2009), no. 6, p. 1203-1217.
[28] J.-M. Cherfils, "Développements et applications de la méthode SPH aux écoulements visqueux à surface libre", PhD Thesis, Université du Havre, 2011.
[29] M. Antuono, A. Colagrossi, S. Marrone, D. Molteni, "Free-surface flows solved by means of SPH schemes with numerical diffusive terms", *Comput. Phys. Commun.* **181** (2010), no. 3, p. 532-549.
[30] P. Randles, L. Libersky, "Smoothed particle hydrodynamics: some recent improvements and applications", *Comput. Meth. Appl. Mech. Eng.* **139** (1996), no. 14, p. 375-408.
[31] M. Antuono, A. Colagrossi, S. Marrone, "Numerical diffusive terms in weakly-compressible SPH schemes", *Comput. Phys. Commun.* **183** (2012), no. 12, p. 2570-2580.
[32] J. Monaghan, R. Gingold, "Shock simulation by the particle method SPH", *J. Comput. Phys.* **52** (1983), p. 374-389.
[33] A. Poupardin, G. Perret, G. Pinon, N. Bourneton, E. Rivoalen, J. Brossard, "Vortex kinematic around a submerged plate under water waves. Part I: Experimental analysis", *Eur. J. Mech. B Fluids* **34** (2012), no. 0, p. 47-55.
[34] J. Monaghan, "Simulating free surface flows with SPH", *J. Comput. Phys.* **110** (1994), no. 2, p. 399-406.
[35] J. Monaghan, "Smoothed particle hydrodynamics", *Rep. Prog. Phys.* **68** (2005), no. 8, p. 1703-1759.
[36] E. P. Mansard, E. R. Funke, "The measurement of incident and reflected spectra using a least squares method", in *Coast. Eng.*, 1980, p. 154-172.
[37] D. G. Goring, "Tsunamis–the propagation of long waves onto a shelf", PhD Thesis, California Institute of Technology Pasadena, California, 1978.
[38] J. Boussinesq, "Théorie des ondes et des remous qui se propagent le long d'un canal rectangulaire horizontal, en communiquant au liquide contenu dans ce canal des vitesses sensiblement pareilles de la surface au fond", *J. Math. Pures Appl.* **17** (1872), no. 2, p. 55-108.
[39] J. V. Wehausen, E. V. Laitone, *Surface Waves*, Springer, 1960.
[40] L. Rayleigh, "On waves", *Phil. Mag.* **1** (1876), no. 5, p. 257-279.
[41] H. Power, A. T. Chwang, "On reflection of a planar solitary wave at a vertical wall", *Wave Motion* **6** (1984), no. 2, p. 183-195.

[42] J. Bougis, "Les houles périodiques simples", Tech. report, Institut des Sciences de l'Ingénieur de Toulon et du Var (ISITV) De l'Université de Toulon et du Var, 1993.
[43] J. McCowan, "Xxxix. on the highest wave of permanent type", *Lond. Edinb. Dublin Phil. Mag. J. Sci.* **38** (1894), no. 233, p. 351-358.
[44] J. Chambarel, "Étude des vagues extrêmes en eaux peu profondes", PhD Thesis, Université de Provence-Aix-Marseille I, 2009.
[45] J. Chambarel, C. Kharif, J. Touboul, "Head-on collision of two solitary waves and residual falling jet formation", *Nonlinear Process. Geophys.* **16** (2009), no. 1, p. 111-122.
[46] J. G. Byatt-Smith, "An integral equation for unsteady surface waves and a comment on the Boussinesq equation", *J. Fluid Mech.* **49** (1971), no. 04, p. 625-633.
[47] Y. Chen, C. Kharif, J. Yang, H. Hsu, J. Touboul, J. Chambarel, "An experimental study of steep solitary wave reflection at a vertical wall", *Eur. J. Mech. B Fluids* **49** (2015), p. 20-28.
[48] G. Oger, P. Guilcher, E. Jacquin, L. Brosset, J. Deuff, D. Le Touzé *et al.*, "Simulations of hydro-elastic impacts using a parallel SPH model", *Int. J. Offshore Polar Eng.* **20** (2010), no. 3, p. 181-189.
[49] Y.-M. Scolan, O. Kimmoun, H. Branger, F. Remy *et al.*, "Nonlinear free surface motions close to a vertical wall. influence of a local varying bathymetry", in *22nd Int. Workshop on Water Waves and Floating Bodies*, 2007.
[50] O. Kimmoun, Y. Scolan, Š.. Malenica *et al.*, "Fluid structure interactions occuring at a flexible vertical wall impacted by a breaking wave", in *The Nineteenth International Offshore and Polar Engineering Conference, International Society of Offshore and Polar Engineers*, 2009.
[51] A. Khayyer, H. Gotoh, H. Falahaty, Y. Shimizu, "An enhanced ISPH–SPH coupled method for simulation of incompressible fluid–elastic structure interactions", *Comput. Phys. Commun.* **232** (2018), p. 139-164.
[52] O. Kimmoun, A. Ratouis, L. Brosset, "Sloshing and scaling: experimental study in a wave canal at two different scales", in *Proceedings of 20th International Offshore and Polar Engineering Conference*, 2010, p. 20-26.
[53] X. Z. Lu, J.-M. Cherfils, G. Pinon, E. Rivoalen, J. Brossard, "SPH Numerical computations of wave impact onto a vertical wall", in *9th International SPHERIC Workshop, Paris, France*, 2014.
[54] X. Lu, "Simulations numériques de l'action de la houle sur des ouvrages marins dans des conditions hydrodynamiques sévères", PhD Thesis, Normandie Université, thèse de doctorat, 2016, http://www.theses.fr/2016LEHA0012/document.
[55] P. Hull, G. Mller, "An investigation of breaker heights, shapes and pressures", *Ocean Eng.* **29** (2002), no. 1, p. 59-79.
[56] C. E. Synolakis, E. N. Bernard, "Tsunami science before and beyond boxing day 2004", *Philos. Trans. Royal Soc. A* **364** (2006), no. 1845, p. 2231-2265.
[57] O. Kimmoun, Y.-M. Scolan, Z. Mravak, "Séminaire clarom océano-météo et hydrodynamique 2008", in *MINISLO*, 2008.
[58] D. Meringolo, A. Colagrossi, S. Marrone, F. Aristodemo, "On the filtering of acoustic components in weakly-compressible SPH simulations", *J. Fluids Struct.* **70** (2017), p. 1-23.
[59] G. Bullock, A. Crawford, P. Hewson, M. Walkden, P. Bird, "The influence of air and scale on wave impact pressures", *Coast. Eng.* **42** (2001), no. 4, p. 291-312.
[60] M. Batlle Martin, G. Pinon, J. Reveillon, O. Kimmoun, "Computations of soliton impact onto a vertical wall: Comparing incompressible and compressible assumption with experimental validation", *Coast. Eng.* **164** (2021), article no. 103817, https://doi.org/10.1016/j.coastaleng.2020.103817.